



## RESEARCH ARTICLE OPEN ACCESS

# Application of Neural Networks for Advanced Ir Spectroscopy Characterization of Ceria Catalysts Surfaces

Mehrdad Jalali<sup>1,2</sup>  | Lachlan Caulfield<sup>1</sup> | Eric Sauter<sup>1</sup> | Alexei Nefedov<sup>1</sup> | Chengwu Yang<sup>3</sup> | Christof Wöll<sup>1</sup> 

<sup>1</sup>Institute of Functional Interfaces, Karlsruhe Institute of Technology, Eggenstein-Leopoldshafen, Germany | <sup>2</sup>Applied Data Science and Artificial Intelligence, SRH University Heidelberg, Heidelberg, Germany | <sup>3</sup>State Key Laboratory of Coal Conversion, Institute of Coal Chemistry, Chinese Academy of Sciences, Taiyuan, China

**Correspondence:** Christof Wöll ([Christof.Woell@kit.edu](mailto:Christof.Woell@kit.edu))

**Received:** 11 March 2025 | **Revised:** 3 June 2025 | **Accepted:** 16 June 2025

**Funding:** Deutsche Forschungsgemeinschaft, Grant/Award Number: 426888090-SFB 1441

**Keywords:** cerium oxide (CeO<sub>2</sub>) | convolutional neural network (CNN) | infrared (IR) spectroscopy | predictive accuracy | surface sites | synthetic data generation

## ABSTRACT

This study presents a novel convolutional neural network (CNN) architecture that represents a significant advancement in the unsupervised analysis of data from infrared (IR) spectroscopy, both in IRRAS (infrared reflection absorption spectroscopy) and in DRIFTS (diffuse reflection infrared Fourier transform spectroscopy). After measuring reference data for single-crystal samples using IRRAS, DRIFTS allows the characterization of surfaces exposed by cerium oxide powder particles through the stretch frequency of adsorbed probe molecules. To enable real-time monitoring of catalyst modification during exposure to reactive gases under reaction conditions, a rapid, unsupervised analysis of the DRIFTS data is required. It is demonstrated that this goal can be achieved by using a CNN with an optimized architecture. This model is proficient in determining the intensities of the adsorbed CO bands, which depend on the crystallographic orientation and oxidation state of the exposed facets. The CNN design incorporates parallel 1D convolutional layers with varied kernel sizes. These layers work in tandem to capture spectral features. To address the challenge of overfitting, advanced regularization techniques within the CNN are integrated, enhancing the model's performance on new, unseen data. In particular, this approach to generating synthetic data has been instrumental in improving the performance of the CNN. The employment of the Adam optimizer and the mean squared error loss function aligns the model for efficient learning, ensuring accurate and reliable predictions. By introducing this CNN architecture, a robust, precise, and adaptable tool for rapid, unsupervised spectroscopic analysis is provided, demonstrating the potential of deep learning combined with synthetic data generation for advanced spectroscopy applications.

## 1 | Introduction

Characterizing oxide powders under ambient conditions and at elevated temperatures is crucial in materials science due to their significant role in catalysis and fuel cells, as well as biomedical and UV protection applications [1–5]. For most oxides, the surface structure exposed by the powder particles and, in particular, the concentration of oxygen vacancies ( $O_v$ ) play a crucial role in their corresponding technical applications. Infrared (IR) spectroscopy, particularly the DRIFTS (diffuse reflection infrared

Fourier-transform spectroscopy) technique, which involves probing molecules adsorbed on the surface of powder particles, offers a nondestructive and insightful approach to investigating the structure of exposed oxide surfaces. A popular example is the carbon monoxide (CO) molecule, which monitors the nature of the adsorption site [6] with remarkable sensitivity. Adsorbed CO exhibits shifts in the stretch frequency that directly correlate with the surface chemistry and morphology and is also sensitive to oxide surface reduction [7]. CO adsorbed on well-defined oxide single crystals shows only a few narrow, individual vibrational

This is an open access article under the terms of the [Creative Commons Attribution](https://creativecommons.org/licenses/by/4.0/) License, which permits use, distribution and reproduction in any medium, provided the original work is properly cited.

© 2025 The Author(s). *Advanced Intelligent Discovery* published by Wiley-VCH GmbH.

bands. In spite of the known fact that advanced theoretical approaches do not allow to assign IR spectra directly (the difference between experimental and calculated values can be up to  $20\text{ cm}^{-1}$ ), calculated values of relative shifts between individual vibrational bands for specific surface orientations and oxidation states fit pretty well to the experimental data, and they make the assignment of the IR spectra obtained on well-defined oxide single crystals straightforward. Unfortunately, the interpretation of the IR spectra recorded for powder particles can be complex, as technologically relevant powders typically contain particles exposing different crystallographic surfaces. As a result, instead of individual peaks, broader bands are observed in the IR spectra, and the analysis demands sophisticated deconvolution techniques to determine the contributions of the different crystallographic planes and their reduction states [8].

The advent of convolutional neural networks (CNN) in processing and analyzing spectroscopic data has recently been used for spectroscopic data analysis [9–12]. CNNs, with their ability to extract and learn from patterns in data, offer unparalleled precision in identifying and predicting the spectral features associated with CO adsorbed on oxide surfaces, both oxidized and reduced. In this article, we focus on the case of  $\text{CeO}_2$ , a material for which experimental results of CO adsorbed on all low-indexed surface orientations is available [13], as well as a thorough theoretical assignment of the CO stretch frequencies. We demonstrate that our CNN is capable of determining the morphologies and oxidation states of  $\text{CeO}_2$  powder particles under reaction conditions, thus allowing us to monitor the state of oxide catalysts in real-world applications [14–17]. Yu et al. applied deep learning for the surface characterization of cerium oxide catalysts utilizing IR spectroscopy of adsorbed CO [18]. Their study demonstrates the efficacy of a CNN model in predicting the distributions of  $\text{CeO}_2$  facets and adsorbed species, utilizing synthetic complex IR spectrum data to enhance predictive accuracy. However, as pointed out by Lustemberg et al. [19], the training data used in this study were obtained from quantum chemical calculations of insufficient performance, thus limiting the performance of the proposed analysis. In the present approach, the training is based on precise experimental data obtained for different  $\text{CeO}_2$  model systems, which were interpreted using accurate quantum-chemical DFT calculations involving hybrid functionals [13].

In another, related work, Saghi et al. present a novel approach to semi-synthetic data generation aimed at fine-tuning CNNs for retrieving Raman signals from coherent anti-Stokes Raman scattering (CARS) spectra [20]. This method not only facilitates the reliable analysis of Raman signals but also highlights the adaptability of CNN models to various spectroscopic data types, reinforcing the versatility of deep learning in spectral analysis. Teklemariam et al. explore the detection of adulteration in coconut water, demonstrating the application of machine and deep learning models, including a 1D CNN with attenuated total reflection-Fourier transform Infrared (ATR-FTIR) spectroscopy. Their work provides insights into the predictive performance of CNNs and other algorithms on spectral data, offering a robust framework for detecting substitutions in food products [21]. Xin et al. investigate the combination of near-IR spectroscopy with generative adversarial networks (GANs) to rapidly detect raw material quality in formula products [22]. Their research on generating synthetic data resembling raw spectral data and

establishing various prediction models exemplifies the potential of integrating GANs with CNN for quality assessment.

Despite these advancements, using CNNs in IR spectroscopy for  $\text{CeO}_2$  powders faces two primary challenges. Firstly, reliable data are only available for the low-indexed crystallographic surfaces, three in the case of  $\text{CeO}_2$ , which significantly reduces the size of the data set necessary for training the CNN. This fact severely hinders the predictive accuracy and generalization capabilities of the CNNs. Secondly, identifying the most effective neural network architecture that can accurately model the complex relationships between IR spectral features remains an ongoing challenge.

To address these challenges, our study focuses on generating synthetic data that accurately simulates the spectral signatures of CO/ $\text{CeO}_2$  IRRAS and DRIFTS data obtained using the so-called SLIR approach [7]. This procedure offers a cost-effective solution to the data scarcity problem, enabling the comprehensive evaluation of the performance of CNN architectures in predicting vibrational spectra of CO adsorbed on  $\text{CeO}_2$  powder particles. By leveraging synthetic data, we aim to refine the training process of CNNs, enhancing their predictive accuracy and reliability. Furthermore, our exploration into identifying the best-fitted CNN architecture for this application intends to set a new benchmark in the field, facilitating more precise and efficient surface characterization of oxide powder particles.

In this study, we synergize the experimental insights from Yang et al., who determined surface faceting and reconstruction of ceria nanoparticles from shifts of the stretch frequency of adsorbed CO, with the work presented in [23] focusing on advanced computational methods to predict CO stretch frequencies theoretically. Yang et al.'s experimental investigations into the CO adsorption on various  $\text{CeO}_2$  model substrates [14] provide a critical experimental foundation, while Lustemberg et al. contribute significantly to the reliable assignment of observed frequencies using advanced computational methods [19]. Finally, in order to test its applicability beyond single-crystal data, our CNN model is extended to DRIFTS data obtained for  $\text{CeO}_2$  powder samples [23]. By integrating these experimental and computational perspectives, our research aims to refine the accuracy of predicting surface phenomena on ceria nanoparticles, illustrating the interplay between experimental validation and computational predictions in material science advancements.

## 2 | Synthetic Data Generation for Enhanced IR Spectroscopy Analysis of $\text{CeO}_2$

In our study, synthetic data generation emerges as a crucial strategy for enhancing the diversity and volume of datasets necessary for training CNNs. This approach is mandatory in domains where experimental data is scarce or prohibitively expensive. Focused on synthesizing IR spectroscopy data, our research aims to simulate the spectral signatures CO adsorbed on cerium oxide surfaces under various conditions. Such synthetic datasets facilitate a thorough exploration of the CNN's ability to identify and predict the surface characteristics of  $\text{CeO}_2$  catalysts, leveraging its notable catalytic properties. Taking in to account the comment

by Lustemberg et al. [19], for CNN training, we used experimentally determined frequencies, and not the results from nonvalidated DFT calculations. In this approach to generating realistic IR spectra for CO adsorbed on CeO<sub>2</sub>, we adopt an innovative algorithm that constructs the spectra by summing Gaussian distributions, each set with a fixed width parameter of  $w = \sqrt{10} \text{ cm}^{-1}$ . These distributions signify the unique vibrational CO stretch frequencies pertinent to specific CeO<sub>2</sub> surface sites on oxidized and reduced particles, based on the core principle that IR spectra of adsorbed CO consist of a superposition of peaks with Gaussian profiles, each corresponding to a distinct molecular vibrational frequency. To further enhance the efficiency of the training process, we incorporate a noise level of 0.15 into our synthetic data, effectively simulating the random variations typical in experimental spectral data. The inclusion of noise emulation is found to be crucial for enhancing the performance of the CNN-based analysis of the experimental data.

Given a range of wavenumbers, the synthetic IR spectrum,  $S(x)$ , is constructed by summing Gaussian distributions for  $N$  CO stretch frequencies. The Gaussian function for the  $i$ -th vibrational mode at a point  $x$  in the wavenumber range is defined as

$$G(x; c_i, a_i, w) = a_i \exp\left(-\frac{(x - c_i)^2}{2w^2}\right)$$

where  $c_i$  represent the center frequency,  $a_i$  the amplitude of the  $i$ -th vibrational mode,  $w$  the width parameter indicating the peak's spread, and  $x$  a value in the wavenumber range  $X$ .

Leveraging our synthetic data generation methodology for IR spectroscopy analysis, this study introduces an enhanced performance in simulating CO/CeO<sub>2</sub> spectra through the strategic

implementation of intensity ratios corresponding to specific frequencies. In our analysis, we consider three primary surface orientations of CeO<sub>2</sub>: the (110), (100), and (111) surfaces, each available in both oxidized and reduced states. These states are crucial as they significantly influence the vibrational frequencies of adsorbed CO molecules, reflecting the varied surface chemistries resulting from the presence of O-vacancies. The next intensity ratios to key frequencies, such as [1.0] for both the 2154 cm<sup>-1</sup> (oxidized state) and 2162 cm<sup>-1</sup> (reduced state) frequencies of the CeO<sub>2</sub> (111) as well as for the 2175 cm<sup>-1</sup> frequency representing the reduced state of the CeO<sub>2</sub> (110) surface, have been applied. For the CeO<sub>2</sub> (110)<sub>ox</sub> state, the ratios of [0.9, 0.3] for frequencies 2171 and 2160 cm<sup>-1</sup> as well as [1.0, 0.4, 0.2] for the complex interaction within the CeO<sub>2</sub> (100)<sub>ox</sub> state at frequencies 2176, 2168, and 2147 cm<sup>-1</sup> as well as [1.0, 0.3] for the CeO<sub>2</sub> (100)<sub>ox</sub> state at frequencies 2168 and 2147 cm<sup>-1</sup> were used. These spectra not only capture the fundamental peaks of CO but can also be generated in numbers large enough to allow for training the CNN. Detailed frequency data and intensity ratios for these interactions are systematically cataloged in Table 1 providing a foundational reference for our spectral analysis.

The generation of synthetic spectra with an optimized noise contribution represents a significant advancement in crafting highly detailed and realistic datasets, which is poised to enhance the training and validation processes of convolutional neural networks for spectral analysis. By intricately mapping these intensity ratios of CO stretch frequencies to the respective oxidation states and surface orientations of CeO<sub>2</sub>, our synthetic datasets are equipped to capture the essential spectral variations. Consequently, this enhances the predictive accuracy and reliability of CNN models in identifying and characterizing material surfaces, underpinning a substantial improvement in the fields of materials science and machine learning.

**TABLE 1** | CO stretch vibration frequencies for different CeO<sub>2</sub> facets and oxidation states.

CeO <sub>2</sub> facets	Oxidation state	Number of CO species	CO frequency (cm <sup>-1</sup> )	Intensity ratios	Description
{110}	Red	1	2175	[1.0]	Represents the reduced state of the CeO <sub>2</sub> (110) surface
{110}	Ox	2	2171, 2160	[0.9, 0.3]	Corresponds to the oxidized state of the CeO <sub>2</sub> (110) surface, also reflecting additional CO stretch frequencies due to complex surface interactions
{100}	Red	2	2168, 2147	[1.0, 0.3]	Denotes the reduced state of the CeO <sub>2</sub> surface on the (100) plane, highlighting the impact of surface reduction on spectral features
{100}	Ox	3	2176, 2168, 2147	[1.0, 0.4, 0.2]	Indicates the oxidized state of the CeO <sub>2</sub> (100) surface showcasing the versatility in surface chemistry and including complex interactions and modifications
{111}	Red	1	2162	[1.0]	Represents the reduced form of the CeO <sub>2</sub> (111) surface, a common facet in nanoparticles
{111}	Ox	1	2154	[1.0]	Pertains to the oxidized state of the CeO <sub>2</sub> (111) surface illustrating the oxidative stability of this facet

The synthetic spectrum  $S(x)$  over the range  $X$  is the sum of Gaussian functions for all considered CO stretch frequencies

$$S(x) = \sum_{i=1}^N G(x; c_i, a_i, w)$$

However, to simulate the effect of experimental noise on the generated spectrum, noise is added to the sum of these Gaussian functions after they are computed. The noise is not part of the Gaussian function itself but is superimposed on the final spectrum. If  $S(x)$  represents the sum of Gaussian functions for all considered CO stretch frequencies, the final synthetic spectrum with noise,  $S_{\text{noise}}(x)$ , can be expressed as

$$S_{\text{noise}}(x) = S(x) + \text{Noise}$$

where Noise is generated from a normal distribution with a mean of 0 and a standard deviation corresponding to the specified noise level (in this case, 0.15). This process effectively models the random fluctuations observed in real spectral data due to various factors, including instrumental noise and environmental variations. Thus, while the Gaussian formula itself remains unchanged, the addition of noise is a critical step in producing a more realistic synthetic spectrum.

A pivotal aspect of our synthetic spectrum generation algorithm is the utilization of specific vibrational frequencies correspond to various CeO<sub>2</sub> facets and oxidation states, as listed in Table 1.

A synthetic dataset is generated by repeating the spectrum construction process, varying  $a_i$  and  $c_i$  within realistic limits to simulate a wide range of possible material responses. This meticulous selection of frequencies enables the generation of synthetic spectra that closely resemble experimental data, encompassing a broad spectrum of potential material responses.

## 2.1 | Synthetic Spectra Generation Process

- I. Initialization: Define a set of center frequencies corresponding to the CO stretch frequencies of interest and a width parameter for the Gaussian distributions to simulate the broadening effect typical in IR spectroscopy.
- II. Single spectrum simulation: For each vibrational mode, generate a Gaussian distribution based on its amplitude and center frequency. The sum of these distributions forms a single synthetic spectrum, approximating the IR spectrum for a predefined set of CO stretch frequencies.
- III. Complex spectrum construction: To create more complex and realistic spectra, simulate the interaction of multiple CO stretch frequencies. This involves determining specific intensity ratios and frequencies for each mode, reflecting their mutual influence, and simulating different CeO<sub>2</sub> surface sites.
- IV. Dataset compilation: Produce a diverse collection of synthetic spectra by assigning random amplitudes to the Gaussian distributions for each spectrum, thus imitating the variability found in experimental IR data. Generate

several thousand of these spectra to form a comprehensive dataset.

- V. Data application: Utilize the synthetic spectra dataset to train a CNN model to predict CeO<sub>2</sub> surface facets and oxidation states based on spectral data.

Figure 1 presents a collection of synthetic IR spectra generated for CO adsorbed on CeO<sub>2</sub>. These spectra were derived from computational modeling based on experimental frequency values, allowing for a controlled exploration of spectral characteristics. Each spectrum showcases distinctive peaks corresponding to specific stretch frequencies of the adsorbed CO probe molecule. The synthetic spectra, constructed from these inputs, serve as the basis for training the CNN used to analyze spectroscopic data.

Our study integrates experimental and theoretical results for CeO<sub>2</sub> single-crystal model systems with spectroscopic data from powder samples under conditions relevant to catalytic reactions. It provides a robust platform for training machine learning models that can predict material surface characteristics with enhanced accuracy, highlighting the potential of synthetic data in advancing spectroscopy and computational materials science. By integrating algorithmic precision and detailed mathematical modeling, we ensure a comprehensive understanding of CeO<sub>2</sub> surface properties and their implications for catalysis and material research.

## 3 | CNN Architecture for Analysis of IR Data

In our study, we leverage the capabilities of CNNs to analyze and predict the surface sites of cerium oxide from IR spectra recorded for adsorbed CO. The architecture of the CNN model is meticulously designed to extract and interpret the complex features within the IR spectra, enabling the accurate prediction of specific CO stretch frequencies associated with different CeO<sub>2</sub> surface facets and oxidation states. This section provides a detailed overview of the CNN architecture and its components tailored for spectral data analysis.

As indicated in Figure 2, the CNN model is structured to capture the nuanced variations in IR spectral data through a series of

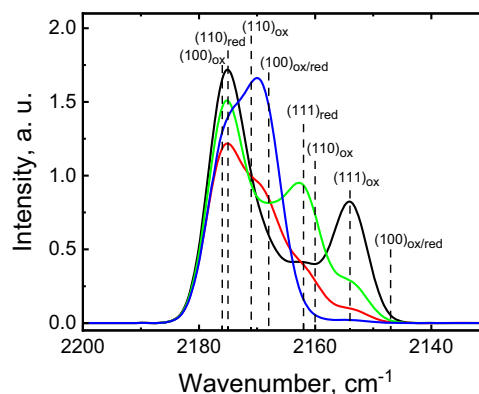


**FIGURE 1** | Four examples of synthetic IR spectra generated for CO adsorbed on different CeO<sub>2</sub> facets. The dashed lines show the positions of IR bands corresponding to CO stretch vibrations (s. Table 1).



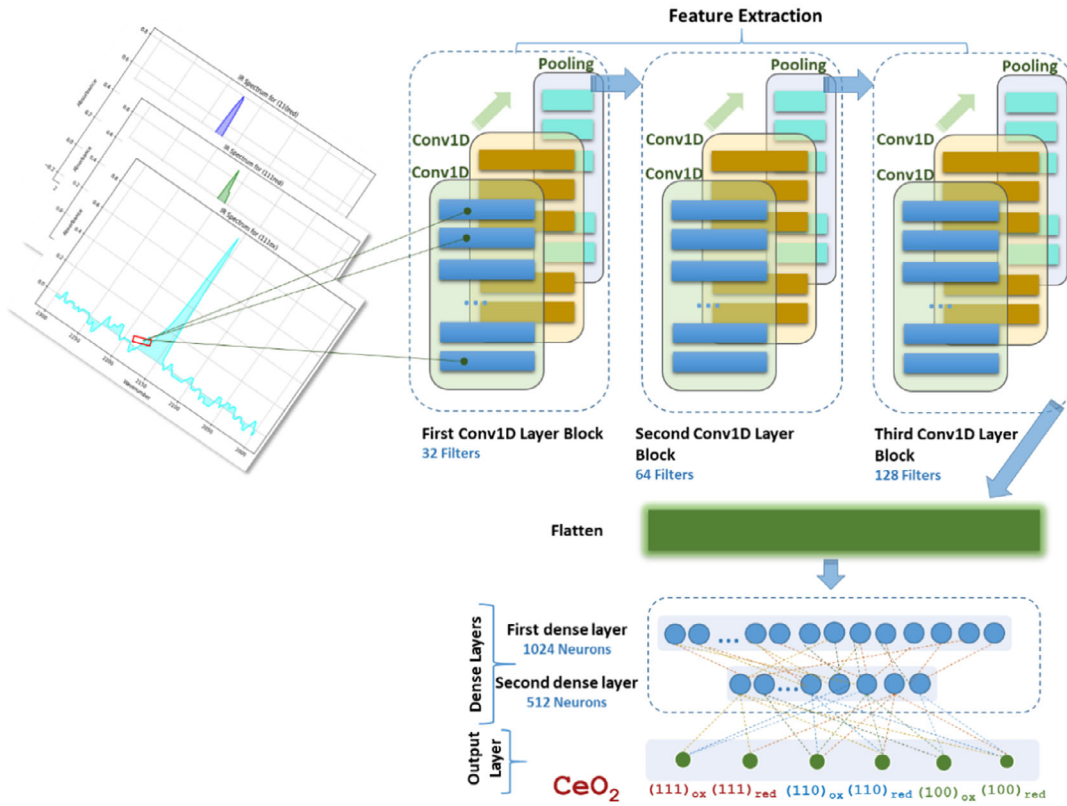


**FIGURE 2** | A scheme of a CNN architecture tailored for 1D spectral data analysis (see the main text for details).

convolutional and dense layers, each serving a distinct purpose in the feature extraction and prediction process. The architecture comprises the following key components:

- **Input Layer:** The model accepts input in the form of reshaped spectra data, with the shape determined by the dimensions of the spectral dataset:

$$X_{input} = X$$

Let's denote the input IR spectra data as  $X \in \mathbb{R}^{m \times n}$ , where  $m$  is the number of samples and  $n$  is the number of features (wavenumbers) per sample.

- **Feature Extraction Stage**

#### A) First Convolutional Block

1. **Convolutional Layer:** For the input spectral data  $X$ , the operation in the first convolutional layer with 32 filters and a kernel size of 5 can be represented as

$$F_1(x) = \text{ReLU}(W_1 * X + b_1)$$

where  $W_1$  represents the weights of the convolutional kernels,  $b_1$  is the bias, and ReLU is the activation function.  $F_1(x)$  denotes the feature maps obtained after this layer. The layer applies L1 regularization, aiming to minimize  $\lambda \sum |W_1|$  where  $\lambda = 0.0001$  is the regularization parameter.

2. **Dropout Layer:** The operation can be considered as a random selection where each neuron output from

$F_1(x)$  has a probability of 0.3 to be set to zero, enhancing the model's generalization.

3. **Second Convolutional Layer:** Applies another set of convolution operations without changing the number of filters or kernel size

$$F_2(x) = \text{ReLU}(W_2 * F_1(x) + b_2)$$

4. **Average Pooling Layer:** This layer reduces the dimensionality by taking the average of every two adjacent values in the feature maps

$$P_1(x) = \text{Pool}_{avg} = (F_2(x))$$

#### B) Second Convolutional Block

1. **Convolutional Layers:** The process is similar to the first block but with an increased number of filters [64]. The operations for the first and second convolutional layers in this block are

$$F_3(x) = \text{ReLU}(W_3 * P_1(x) + b_3)$$

$$F_4(x) = \text{ReLU}(W_4 * F_3(x) + b_4)$$

2. **Dropout:** Applied again with a rate of 0.3 after each convolutional operation.

3. **Average Pooling:** Reduces dimensionality, similar to the first block

$$P_2(x) = Pool_{avg} = (F_4(x))$$

### C) Third Convolutional Block

1. **Convolutional Layers:** This block further increases the filter count to 128, enhancing the model's capacity to capture complex features. The operations are represented as

$$F_5(x) = \text{ReLU}(W_5 * P_2(x) + b_5)$$

$$F_6(x) = \text{ReLU}(W_6 * F_5(x) + b_6)$$

2. **Dropout:** The rate is increased to 0.4 for these layers to prevent overfitting.
3. **Average Pooling:** Completes the block with dimensionality reduction:

$$P_3(x) = Pool_{avg} = (F_6(x))$$

In these expressions,  $W_n$  and  $b_n$  denote the weights and biases of the  $n$ -th convolutional layer, respectively. The ReLU activation function introduces nonlinearity, enabling the detection of complex spectral patterns. The average pooling operations  $Pool_{avg}$  summarize the features, reducing the spatial dimensions of the feature maps and preparing the data for the quantification stage.

- **Flattening** The output from the last pooling layer  $P_3(x)$  is transformed into a one-dimensional vector  $v$ , presubsequent paring it for the dense layers:

$$v = \text{Flatten}(P_3(x))$$

#### – Dense Layer

1. **First Dense Layer:** This layer transforms the flattened vector  $v$  into a high-dimensional space through a dense connection of neurons, featuring 1024 neurons with ReLU activation and L1 regularization

$$D_1(v) = \text{ReLU}(W_{d1} * v + b_{d1})$$

2. **Dropout:** To reduce overfitting, a dropout layer with a rate of 0.5 is applied after the first dense layer.
3. **Second Dense Layer:** Applies a transformation similar to the first dense layer but reduces the dimensionality to 512 neurons

$$D_2(v) = \text{ReLU}(W_{d2} * v + b_{d2})$$

4. **Dropout:** A second dropout layer with a rate of 0.5 follows the second dense layer to further mitigate the risk of overfitting.

- **Output Layer** The final layer in the model predicts the amplitudes for the specific frequencies. The number of neurons in this layer matches the number of specific frequencies ( $n$ ), with each neuron's output corresponding to an amplitude prediction

$$Y = \text{ReLU}(W_{\text{out}} * D_2(v) + b_{\text{out}})$$

Here,  $W_{\text{out}}$  and  $b_{\text{out}}$  are the weights and biases of the output layer, respectively. This layer also incorporates L1 regularization.

- **Optimization** The model uses the Adam optimizer with a learning rate of 0.0001, focusing on minimizing the mean squared error (MSE) between the predicted amplitudes  $Y$  and the actual amplitudes  $Y_{\text{true}}$

$$\text{Loss} = \frac{1}{m} \sum_{i=1}^m (Y_i - Y_{\text{true}i})^2$$

where  $m$  is the number of samples.

This study unveils an innovative CNN architecture specialized for the analysis, crafted to analyze specific frequency amplitudes. The architecture features a carefully structured series of convolutional layers, starting with 32 and scaling up to 128 filters, combined with L1 regularization (parameter 0.0001) to combat overfitting, enabling it to handle the intricate patterns found in spectral data. Initially, we experimented with simpler CNN models, but these attempts fell short, failing to accurately reproduce the experimental data. This revealed a critical insight: the complexity of spectroscopic signals requires more than basic CNN models. We invested considerable time refining the architecture, moving beyond simple models to craft a more sophisticated, high-performing solution. This enhanced CNN transitions from feature extraction—utilizing dropout techniques and average pooling for data refinement—to dense layers with 1024 and 512 neurons, thereby ensuring precise amplitude predictions. Adam, which is an adaptive learning rate method designed to update network weights iteratively based on training data, with a learning rate of 0.0001 and focused on minimizing mean squared error, was used for the optimization. The final model represents a major leap forward in spectroscopic analysis; it blends precision with robustness, offering a scalable, flexible tool poised to redefine material characterization through deep learning.

Two types of neural networks were trained: a CNN and a deep neural network (DNN), using 5000 synthetic spectra, and then tested on 1000 new spectra. The DNN we designed consists of two main layers, each with 91 and 96 units, and utilizes a specific setting (a regularization parameter of 0.001) to prevent the model from overfitting the data, which can be a problem. This setup was chosen to enhance the DNN's ability to learn from complex patterns in the data. We measured the predictive accuracy of these models using the root mean squared error (RMSE) and the  $R^2$  Score, which indicate how accurately the models predict outcomes and how well they explain the differences in the data. RMSE measures the differences between values predicted by a model and observed values. For the proposed CNN architecture,

after calculating the MSE loss function Loss as defined, RMSE can be calculated from MSE. Given that Loss represents the MSE

$$\text{RMSE} = \sqrt{\text{Loss}} = \sqrt{\frac{1}{m} \sum_{i=1}^m (Y_i - Y_{\text{true}i})^2}$$

where  $Y$  represents the predicted amplitudes,  $Y_{\text{true}}$  represents the actual amplitudes associated with the IR spectra, and  $m$  is the number of samples.

The  $R^2$  score, or coefficient of determination, measures how well the observed outcomes are replicated by the model based on the proportion of total variation of outcomes explained by the model

$$R^2 = 1 - \frac{SS_{\text{res}}}{SS_{\text{tot}}}$$

where  $SS_{\text{res}}$  is the sum of squares of the residual errors ( $SS_{\text{res}} = \sum (Y_i - Y_{\text{true}i})^2$ ), and  $SS_{\text{tot}}$  is the total sum of squares or total variance in the data ( $SS_{\text{tot}} = \sum (Y_i - \bar{Y})^2$ ), where  $\bar{Y}$  is the mean of actual values.

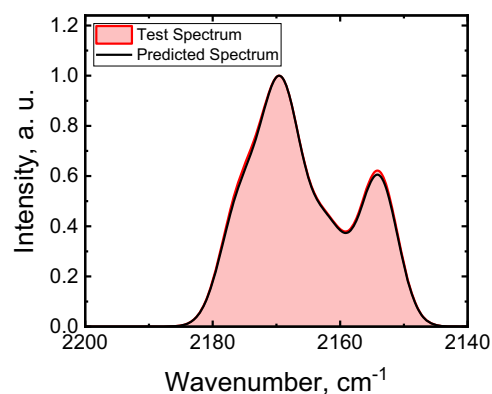
The results are shown in Table 2. The CNN performed significantly better, with a lower RMSE and a higher  $R^2$  Score, than the deep neural network. This means that CNN was more accurate in picking up and interpreting the complex patterns in the synthetic data. Although the DNN was carefully constructed, with its specific layer set designed to prevent overfitting, it did not outperform the CNN in this test.

Figure 3 indicates one example of the comparative results between the actual and predicted IR spectra, which underscores the CNN model's capacity to replicate the essential features of IR spectral data accurately. Notably, the model exhibits a remarkable ability to capture most IR spectral characteristics that correspond to  $\text{CeO}_2$  facets, which is evident in the consistent alignment of the spectral peaks across the plots. This alignment is critical, as the peaks represent the CO stretch frequencies specific to the  $\text{CeO}_2$  crystal facets and indicate the material's surface sites. The close matching of spectra in the peak regions across multiple samples validates the model's robustness and suggests its applicability in distinguishing different  $\text{CeO}_2$  surface structures. The precision of the model in these regions, where the most significant spectral features occur, demonstrates its potential as a reliable tool for analyzing and interpreting IR spectroscopy data, with specific implications for advancing  $\text{CeO}_2$  facet analysis and understanding CO adsorption effects.

**Evaluating CNN model resilience to noise in spectral data analysis:** In our research, we investigated the resilience of a CNN model to various levels of noise in spectral data analysis,

**TABLE 2** | Comparative performance of CNN and DNN models in spectroscopic data analysis.

Prediction task	RMSE	$R^2$ score
CNN	0.011	0.999
DNN	0.124	0.809



**FIGURE 3** | Test (area) vs. predicted (black line) IR spectrum using the CNN model. The test spectrum is synthetically generated using Gaussian distributions with CO stretch frequencies from Table 1, random amplitudes, and 0.15 noise, showing accurate replication of CO/ $\text{CeO}_2$  spectral features.

a critical factor for its deployment in real-world scenarios affected by measurement inaccuracies and environmental disturbances. By synthesizing spectral data infused with Gaussian noise ranging from light (0.1) to heavy (0.8), we systematically assessed the model's accuracy using metrics such as root mean squared error (RMSE) and R-squared ( $R^2$ ) score. Our findings revealed that while the model exhibits commendable predictive reliability at lower noise intensities, a marked decline in accuracy was observed with increasing noise levels. This underlines the importance of incorporating sophisticated noise management techniques to bolster the model's predictive proficiency across a broader spectrum of noise conditions. Figure 4 visually contrasts actual vs. predicted noise impacts for three sample spectra, and Table 3 summarizes the differential impact on RMSE and  $R^2$  Scores across noise levels, thereby emphasizing the model's practical utility and the imperative for enhanced noise mitigation strategies.

**Experimental evaluation of the CNN model:** In our previous [14, 24, 25], we extensively investigated the vibrational frequencies of CO adsorbed on various facets of cerium oxide ( $\text{CeO}_2$ ) by using different single crystals as model systems. This inquiry is

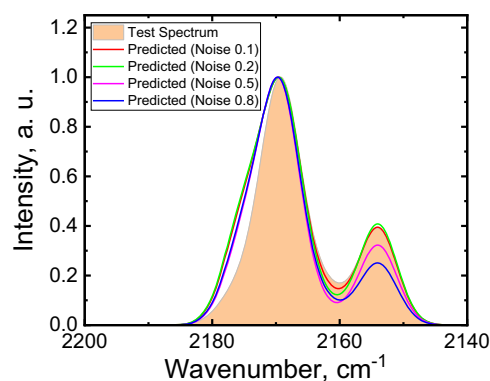


**FIGURE 4** | Test vs. predicted IR spectra at noise levels (0.1–0.8). Test spectra are synthetically generated using Gaussian distributions with CO stretch frequencies from Table 1, random amplitudes, and varying noise, demonstrating the CNN's robustness to noise.

**TABLE 3** | Performance metrics of the CNN model at various noise levels, demonstrating the impact of Gaussian noise on predictive accuracy through RMSE and  $R^2$  scores.

Noise level	RMSE	$R^2$ score
0.1	0.146	0.859
0.2	0.159	0.834
0.5	0.222	0.673
0.8	0.281	0.472

crucial for providing reliable reference data for the analysis of the technologically relevant powders, which consist of particles with typical sizes between 10 and 100 nm. These experiments were conducted to obtain IR spectra of adsorbed CO, revealing a clear shift in vibrational frequencies for different  $\text{CeO}_2$  facets. In addition, upon reduction of the oxidized samples, additional shifts in the CO vibrational frequencies were observed. Such reference data, which were interpreted based on state-of-the-art theoretical work, are instrumental in identifying the surface structures of  $\text{CeO}_2$  powder particles, thereby providing an invaluable benchmark for verifying computational models, including CNNs. Using experimental IRRAS datasets from  $\text{CeO}_2$  single crystals, we aim to validate CNN's proficiency in precisely predicting and delineating the intricate vibrational characteristics of CO on ceria surfaces. Achieving this would mark a significant stride forward in enhancing its applicability in the fields of catalysis and surface science.

### • $\text{CeO}_2$ single crystal case

As a starting point in this experimental evaluation, we tested the CNN model's predictive accuracy by comparing its performance when analyzing experimental IRRAS datasets available for three differently oriented  $\text{CeO}_2$  single crystals. The analysis covered both oxidized and reduced states of  $\text{CeO}_2$  surfaces with three low-index crystallographic orientations: (100), (110), and (111) (Figure 5–7). To exclude any contributions resulting from experimental noise, the 10% threshold was established—it means that all bands with an intensity less than 0.1 would not be taken into account in the discussion, and the corresponding distribution plots are presented in light blue color.

The IRRAS measurements, described in this section, were performed under ultra-high vacuum (base pressure  $3 \times 10^{-11}$  mbar) at 65–70 K on well-prepared  $\text{CeO}_2$  single crystals, following the procedure described in Yang et al. [14]. CO was dosed at  $\sim 1 \times 10^{-10}$  mbar in several steps until monolayer saturation was achieved. IR spectra were recorded with a resolution of  $2 \text{ cm}^{-1}$  using a Bruker VERTEX 80v spectrometer with a use of the MCT detector.

For the IRRAS spectrum recorded for the oxidized  $\text{CeO}_2$  (100) surface, the CNN correctly predicts the largest intensity (Figure 5a) for the vibration at  $2176 \text{ cm}^{-1}$ , underscoring the CNN's ability to recognize the spectral features of this oxidized state. The model's distribution plot (Figure 5b) demonstrates the presence of the dominant  $\text{CeO}_2$  (100)<sub>ox</sub> peak. However, relatively

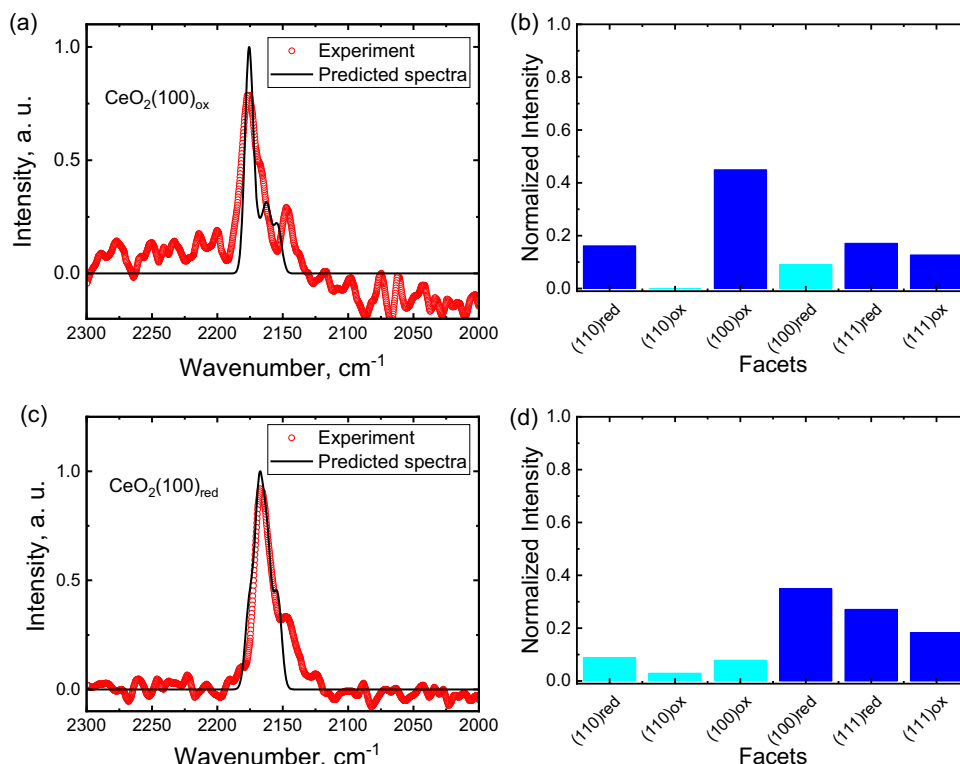


**FIGURE 5** | (a) Experimental vs. predicted spectra for the oxidized  $\text{CeO}_2$  (100) surface, showing a close match at  $2176 \text{ cm}^{-1}$  (predicted at  $2178 \text{ cm}^{-1}$ ). (b) Predicted facet distribution for  $\text{CeO}_2$  (100)<sub>ox</sub>, accurately identifying dominant surface states. (c) Experimental vs. predicted spectra for the reduced  $\text{CeO}_2$  (100) surface, with high alignment around  $2168 \text{ cm}^{-1}$  (predicted at  $2170 \text{ cm}^{-1}$ ). (d) Predicted facet distribution for  $\text{CeO}_2$  (100)<sub>red</sub>, capturing both  $\text{CeO}_2$  (100)<sub>red</sub> and minor  $\text{CeO}_2$  (111) contributions.



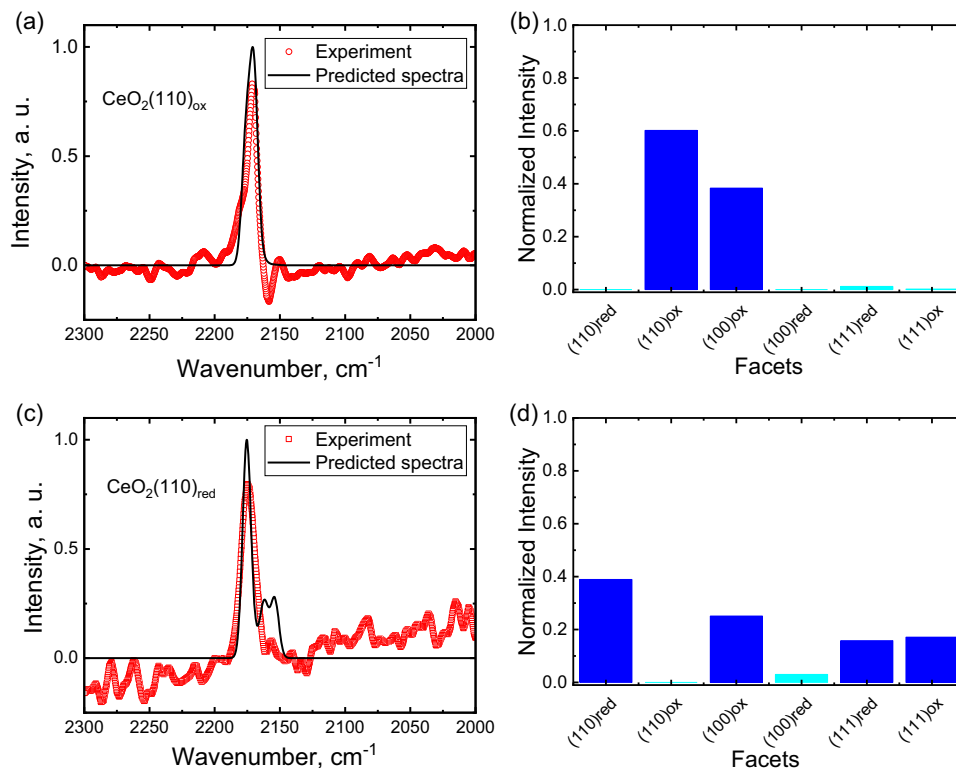


**FIGURE 6** | (a) Experimental vs. predicted absorbance for the oxidized  $\text{CeO}_2(110)$  surface, closely matching at  $2170 \text{ cm}^{-1}$  (predicted at  $2172 \text{ cm}^{-1}$ ). (b) Predicted facet distribution for  $\text{CeO}_2(110)_{\text{ox}}$ , showing dominant surface contributions. (c) Experimental vs. predicted absorbance for the reduced  $\text{CeO}_2(110)$  surface, with strong alignment around  $2175 \text{ cm}^{-1}$  (predicted at  $2177 \text{ cm}^{-1}$ ). (d) Predicted facet distribution for  $\text{CeO}_2(110)_{\text{red}}$ , accurately reflecting reduced surface states.

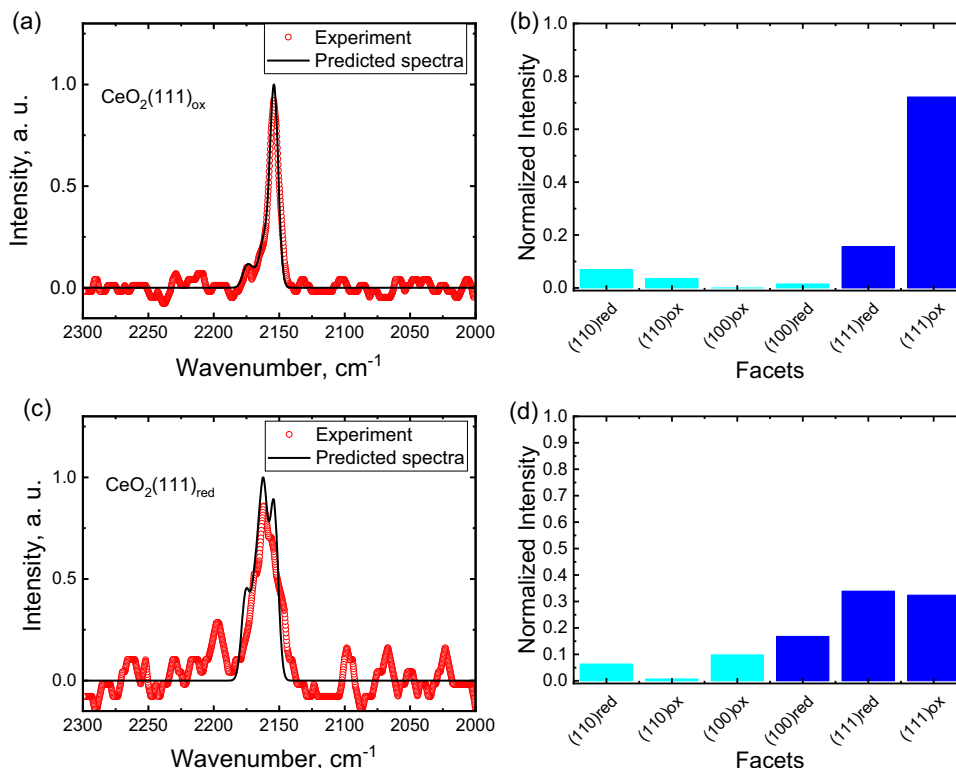


**FIGURE 7** | (a) Experimental vs. predicted absorbance for the oxidized  $\text{CeO}_2(111)$  surface, showing strong alignment at  $2154 \text{ cm}^{-1}$  (predicted at  $2156 \text{ cm}^{-1}$ ). (b) Predicted facet distribution for  $\text{CeO}_2(111)_{\text{ox}}$ , accurately identifying dominant oxidized surface states. (c) Experimental vs. predicted absorbance for the reduced  $\text{CeO}_2(111)$  surface, closely matching at  $2162 \text{ cm}^{-1}$  (predicted at  $2164 \text{ cm}^{-1}$ ). (d) Predicted facet distribution for  $\text{CeO}_2(111)_{\text{red}}$ , reflecting reduced surface contributions.

low contributions (just above and close to the threshold level) for other IR bands are also observed. The appearance of both  $\text{CeO}_2$  (111)<sub>ox</sub>/ $\text{CeO}_2$  (111)<sub>red</sub> contributions with comparable intensity results is tentatively explained by the formation of {111} facets on the  $\text{CeO}_2$  (100)<sub>ox</sub> surface, according to observations reported by Yang et al. [14]. The presence of  $\text{CeO}_2$  (100)<sub>red</sub> component it is not expected for an oxidized  $\text{CeO}_2$  (100) surface. Also, the presence of a  $\text{CeO}_2$  (110)<sub>red</sub> component for this surface is surprising, especially since no  $\text{CeO}_2$  (110)<sub>ox</sub> state is observed. We suppose these results are an artifact of the CNN analysis, since the corresponding states, namely  $\text{CeO}_2$  (100)<sub>red</sub> and  $\text{CeO}_2$  (110)<sub>red</sub>, have frequencies which are very close in energy, 2175, 2168, and 2147  $\text{cm}^{-1}$  the  $\text{CeO}_2$  (100)<sub>ox</sub> state with the bands at 2176, 2168, and 2147  $\text{cm}^{-1}$  (see Table 1). It is a well-known problem for an analysis of experimental data, which could be overcome with a presence of additional information. This example underlines the importance of a proper model for CNN training; otherwise, it can provide wrong predictions, especially for complicated cases, as described above.

For the reduced  $\text{CeO}_2$  (100) surface, the corresponding IRRA spectrum (Figure 5c) closely matched the actual data around 2168  $\text{cm}^{-1}$ , and the CNN effectively predicted a substantial presence of the  $\text{CeO}_2$  (100)<sub>red</sub> state (Figure 5d). Similar to the  $\text{CeO}_2$  (100)<sub>ox</sub> surface, both  $\text{CeO}_2$  (111) states are present as well. These results underscore the model's capability to accurately predict both the presence and spectral features of the reduced state.

The IRRA spectrum (Figure 6a) and the corresponding distribution plot (Figure 6b) for the oxidized  $\text{CeO}_2$  (110) surface demonstrated the model's precision in matching the actual spectrum, particularly around 2170  $\text{cm}^{-1}$ , showcasing effective prediction capabilities. Similarly, IRRA spectrum (Figure 6c) and the distribution for the reduced  $\text{CeO}_2$  (110) (Figure 6d) highlighted the model's accurate predictive ability, especially around 2175  $\text{cm}^{-1}$ . The strong (above threshold) contributions of  $\text{CeO}_2$  (100)<sub>ox</sub> in both distribution plots (Figure 6b,d) are explained with their nearness to positions of the  $\text{CeO}_2$  (110)<sub>ox</sub>/ $\text{CeO}_2$  (110)<sub>red</sub> IR bands. The reasonable  $\text{CeO}_2$  (111)<sub>ox</sub>/ $\text{CeO}_2$  (111)<sub>red</sub> contributions for  $\text{CeO}_2$  (110)<sub>red</sub> state could be also explained with the {111} facet formation, as discussed above.

When assessing the oxidized states of the  $\text{CeO}_2$  (111) surface, the CNN model correctly predicted a high prevalence of the corresponding  $\text{CeO}_2$  (111)<sub>ox</sub> state, as indicated in the IRRA spectrum (Figure 7a) and the corresponding distribution plot (Figure 7b), confirming the model's accuracy through the peak around 2154  $\text{cm}^{-1}$ . The small, but above threshold, contribution of  $\text{CeO}_2$  (111)<sub>red</sub> state is not surprising, because this state was experimentally observed for (almost)-full oxidized  $\text{CeO}_2$  (111) surface. However, for the reduced state of this surface, while the model indicated a substantial presence within the dataset, as shown in the absorbance spectrum comparison (Figure 7c), aligning predicted peaks with actual data around 2162  $\text{cm}^{-1}$ , the precision was not as high as for other states.

To conclude, this detailed examination across different  $\text{CeO}_2$  oxidation states and planes, from Figures 5–7, reveals the CNN model's strength and accuracy in predicting IRRA spectra for all three low-index facets in the oxidized state and for (110) surfaces in the reduced state with high precision. However, it also highlights the

areas where the model's predictions for the (111) and (100) facets in the reduced state did not reach the same level of precision. The latest result is not surprising because all CNN-based predictions have been done for ideally stoichiometric and nonreconstructed surfaces. Thus, on the one hand,  $\text{CeO}_2$  surfaces in the oxidized state are very close to the above-mentioned conditions, resulting in a highly precise prediction. On the other hand,  $\text{CeO}_2$  (100) surface is polar and unstable; during reduction, it is reconstructed with a formation of {111} facets (13), and the CNN could predict this effect as well.

#### • $\text{CeO}_2$ powder case

Extending our CNN model's capabilities to powder samples, specifically  $\text{CeO}_2$  in various oxidation states, underscores its applicability beyond single-crystal data. This section outlines the methodology employed in the experiments. It discusses the results and implications of the CNN model's performance, focusing on the different oxidation states captured in the provided dataset.

The experimental setup was designed to reproduce practical catalytic conditions (quasioperando). Diffuse reflectance IR Fourier transform spectroscopy (DRIFTS) measurements were performed in a VERTEX 80 spectrometer (Bruker) equipped with Praying Mantis diffuse reflection optics (Harrick). The ceria powder used for the experiments was purchased from Sigma-Aldrich. According to scanning electron microscopy (SEM) studies, the powder consisted of irregularly shaped polyhedra that exposed predominantly {111} facets, while differently oriented {110} and {100} facets occurred substantially less frequently. Before DRIFTS measurements, the powders were first cleaned by heating to 700 K in constant  $\text{O}_2$  flow. Spectra were continuously measured upon dosing CO at pressures of 1 bar. To study the time dependence, spectra were recorded every 55 s using a resolution of 2  $\text{cm}^{-1}$ . These measurements continue for more than 1 h, allowing the evolution of the ceria powder to be tracked over time in a reactive atmosphere. The use of a novel subtraction scheme [23] allowed us to unambiguously identify and then remove almost all (~95%) CO gas-phase contributions (ro-vibrational bands). After normalizing the DRIFTS data, the IR bands originating from CO vibrations on the surfaces of ceria powders were clearly identified in these IR spectra (see Figure 8). The low-period oscillations in these spectra correspond to residual traces of the gas-phase ro-vibrational signals. Notably, the broad feature around 2130  $\text{cm}^{-1}$  results from IR-induced electronic transitions localized mostly in the ceria bulk [26–28]. The latter feature is not connected with CO adsorption on ceria surfaces and is not included in CNN-based data analysis. Monitoring the reduction process of the ceria powders in real time required the recording of about one hundred of individual spectra. Such a number of experimental spectra makes a manual fitting procedure a daunting task, and the application of CNN in such experiments is highly desirable.

In Figure 8a–d, a few experimental DRIFTS data sets were measured during CO-induced  $\text{CeO}_2$  reduction at different time points (1, 3.5, 6, and 90 min) on the time scale. Similar to the single-crystal case, the contributions of different facets and oxidation states were predicted for all spectra; the corresponding time dependencies are summarized and presented in Figure 9.

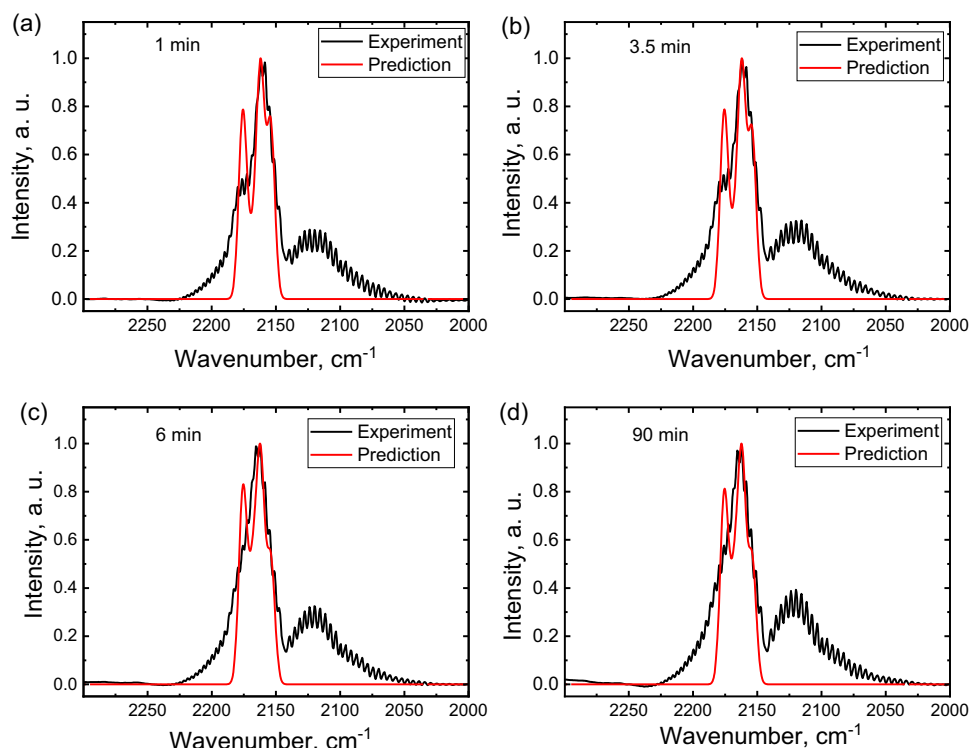


**FIGURE 8** | DRIFT spectra measured at various time points during the CO-induced reduction of  $\text{CeO}_2$  powder.

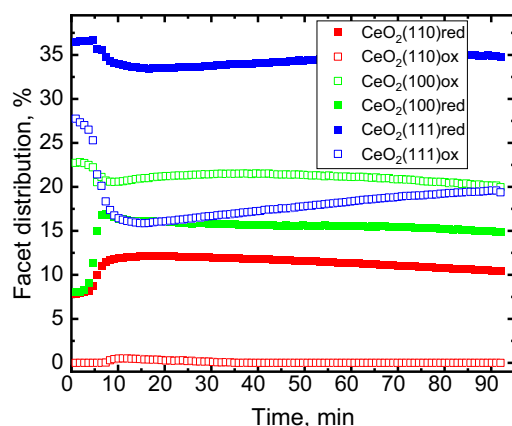


**FIGURE 9** | The temporal evolution of different  $\text{CeO}_2$  surface facets and their oxidation states during CO reduction.

An inspection of the data reveals several new features that were not observed in the IRRAS data for single crystals. Firstly,  $\text{CeO}_2$  powder nanoparticles have more surface structure defects compared to single crystals, resulting in a broadening of all bands in the experimental DRIFTS data. Since the difference between positions of different CO bands is small (e.g.  $1 \text{ cm}^{-1}$  for the  $\text{CeO}_2(110)_{\text{red}}$  and  $\text{CeO}_2(100)_{\text{ox}}$  components) (see Figure 1 and Table 1), this effect introduces a prediction uncertainty when applying the CNN analysis. Secondly, a new band at  $2183 \text{ cm}^{-1}$  is present in all CO/ $\text{CeO}_2$  powder DRIFTS data.

This band has not been observed for well-defined, clean  $\text{CeO}_2$  single crystals but has been reported to occur in CO/ $\text{CeO}_2$  FT-IR spectra, measured on powders before [29–31]. Since this band was not included in the CNN training procedure, the components with positions at high values of wavenumbers, namely

$\text{CeO}_2(110)_{\text{red}}$  and  $\text{CeO}_2(100)_{\text{ox}}$ , could be overestimated. As mentioned above, around  $2130 \text{ cm}^{-1}$ , an additional peak corresponding to IR-excited electronic transitions in bulk ceria is observed. The intensity of this peak is proportional of the reduction degree of the whole sample [32], both of surface and of bulk and, therefore, its intensity is increasing during CO reduction of ceria (see for comparison Figure 8a,d). This increase also affects the CNN prediction. Despite these limitations and the increased uncertainty in  $\text{CeO}_2$  powder data, the main features related to CO adsorbate vibrational bands could be accurately identified. Initially, the vibrational bands corresponding to {111} and {100} facets are clearly identified. As it was mentioned above for the single crystal case (s. Figure 5b), it is not possible to distinguish the  $\text{CeO}_2(100)_{\text{ox}}$  band from the  $\text{CeO}_2(110)_{\text{red}}$  +  $\text{CeO}_2(100)_{\text{red}}$  mixed contribution. This effect results in some underestimation of  $\text{CeO}_2(100)_{\text{ox}}$  predicted value. The high predicted value of  $\text{CeO}_2(111)_{\text{red}}$  component is rather surprising, since at the beginning of the exposure the powders should be fully oxidized. We attribute this effect to the broadening of the experimental peaks in the DRIFTS data, resulting in an additional (apparent) contribution from the  $\text{CeO}_2(111)_{\text{ox}}$  component—the difference in frequency amounts to only  $8 \text{ cm}^{-1}$  (see Table 1). From the time dependence (Figure 9), it is established that the main changes in the contribution of the different CO bands occur within the first 10 min of CO exposure. As the experiment progresses, the intensities of all bands reach a dynamic equilibrium, maintaining steady levels indicative of stabilized surface chemistry. The initial stages exhibit a clear inverse relationship between the oxidized (open symbols) and reduced (filled symbols) states for all facets except  $\text{CeO}_2(111)_{\text{red}}$ , as expected for the CO-induced reduction of the samples. As analyzed through our CNN model, the differing behaviors among the  $\text{CeO}_2$  facets highlight intrinsic variations in stability and reactivity that are

crucial for applications requiring dynamic redox cycling, such as catalysis and environmental sensing. The model's robustness in predicting these facet-specific behaviors under varying oxidation states demonstrates its potential as a predictive tool in material science for CeO<sub>2</sub> powders. It underscores its effectiveness in capturing the complex spectral features of different surface chemistries. This insight is instrumental in facilitating the design of CeO<sub>2</sub>-based materials with tailored properties, where adjusting experimental parameters can optimize facet characteristics, thereby enhancing material performance for specific applications.

The experimental evaluation of the CNN model with CeO<sub>2</sub> powder samples provides compelling evidence of the model's capability to handle complex, real-world material systems. By accurately predicting changes in the oxidation states and providing insights into the stability and reactivity of different facets, the CNN model proves to be an invaluable tool for advancing material science research and applications involving CeO<sub>2</sub> powders.

Despite the model's strong performance in identifying key features in DRIFTS spectra, the complexity of powder samples, such as surface reconstruction, defect-induced peak broadening, and unmodeled bands like the one observed at 2183 cm<sup>-1</sup>—introduces an intrinsic prediction uncertainty. Based on synthetic data parameters ( $\sigma = 10 \text{ cm}^{-1}$ , noise = 0.15), model performance across noise levels (Table 3), and comparisons to experimental spectra, we estimate this uncertainty to be within  $\pm 5\text{--}10 \text{ cm}^{-1}$ . This range is higher than in the single-crystal case and reflects the convolution of experimental variability with model limitations. Future improvements could involve extending the training set to include additional spectral features, such as the 2183 cm<sup>-1</sup> band, to further reduce this error margin.

Our experimental evaluations CeO<sub>2</sub> have consistently demonstrated the robust capability of the CNN model to discern and predict the intricate spectral characteristics of CeO<sub>2</sub> surface states across various experimental datasets. These datasets encompass a range of conditions representing both oxidized and reduced states of CeO<sub>2</sub> and different crystallographic orientations such as (100), (110), and (111). The benefits of the CNN model extend beyond mere prediction accuracy. The model's ability to process and analyze complex data sets derived from synthetic spectra simulates real-world conditions, which often contain irregularities and noise. Furthermore, the model's success in these evaluations offers a clear pathway for its application in continuously monitoring and analyzing CeO<sub>2</sub> powders and other oxides in operational settings. Industries focusing on producing and utilizing catalytic materials can leverage this model to enhance the efficiency and longevity of their catalysts by adjusting operational parameters in real time based on CNN's predictive outputs. These results validate the proposed CNN's design and synthetic training regime and illuminate its potential as a transformative tool for the broader field of materials science. By enabling more precise and predictive analyses, the CNN model helps bridge the gap between theoretical science and practical application, marking a significant step forward in integrating machine learning technologies in material analysis and engineering. We close this paragraph by pointing out that this type of analysis is certainly not limited to CO on ceria, but can be applied to metal deposits on

ceria particles [33] and to other oxides [34]. We would also like to note that this analysis applies to other probe molecules, such as N<sub>2</sub>O, methanol, and O<sub>2</sub>.

This study builds upon recent advances in neural network applications to vibrational spectroscopy. For instance, previous work [35] demonstrated the prediction of vibrational spectra directly from molecular structures, focusing primarily on organic molecules and gas-phase systems. While such structure-to-spectrum approaches offer an efficient alternative to DFT for small molecular systems, our work follows a different direction. Here, we use a CNN to interpret IR spectra of CO adsorbed on ceria surfaces and predict the underlying surface structure and oxidation state. This spectral-to-structure strategy, applied to complex solid-state systems and validated against experimental IRRAS and DRIFTS data, offers a practical and scalable solution for analyzing surfaces with mixed facets or defect-related features, scenarios that are often challenging for conventional DFT-based methods.

## 4 | Conclusions

This research has achieved considerable progress in utilizing CNNs to analyze different types of IR spectroscopy data applied to CO adsorbed on ceria, including IRRAS data recorded for single crystals, data recorded in transmission for powders, and DRIFTS data. This approach allows explicitly identifying the surface sites exposed by cerium oxide (CeO<sub>2</sub>) particles. By developing a novel CNN architecture capable of accurately predicting spectral signatures through the analysis of synthetic data, we have demonstrated a new level of performance in the spectroscopic analysis of CeO<sub>2</sub> surfaces. The synthetic data generation process, rooted in the simulation of IR spectra with Gaussian distributions and defined intensity ratios for specific frequencies, has enabled the creation of extensive datasets that closely mimic real experimental scenarios, thereby overcoming the limitations posed by the scarcity of experimental data.

The integration of parallel 1D convolutional layers with varying kernel sizes within the CNN architecture has been instrumental in capturing the nuances of spectral data across different scales. This approach has enhanced the model's ability to discern intricate spectra patterns and set a new benchmark for the accuracy and efficiency of spectroscopic analysis in material science research. Furthermore, employing advanced regularization techniques has significantly reduced the risk of overfitting, ensuring the model's reliability and robustness in predicting CeO<sub>2</sub> surface sites across diverse conditions.

The promising results of this study pave the way for future research to expand the application of CNNs trained using synthetic data for vibrations of adsorbed probe molecules beyond CeO<sub>2</sub> to a broader range of materials, enhancing the universality and precision of spectroscopic analysis in material science. Future directions will likely focus on refining synthetic data generation methods to incorporate more complex interactions, applying the model to probe molecules different from CO, and for other spectroscopic techniques to facilitate holistic material characterization. Additionally, real-time analysis applications will be explored in industrial and environmental settings.

Additionally, advancements in computational models, including the use of graph learning to represent synthetic data in graph form, the integration of GANs, and transfer learning, are anticipated to improve predictive accuracy and efficiency further, marking a significant leap forward in applying machine learning to materials science research.

Importantly, our results emphasize that CNNs are not designed to replicate or fit IR spectra directly but to extract structural insights, such as surface orientation and oxidation state, from complex or noisy experimental data. Trained on experimentally validated vibrational frequencies, the CNN serves as a complementary tool to traditional DFT-based methods, which often struggle with spectral overlap, low signal intensity, or non-linear backgrounds in real experimental conditions. This approach is particularly valuable for interpreting challenging spectra and enhancing the analysis of surface properties in catalytic materials.

## Acknowledgements

This work was supported by the Deutsche Forschungsgemeinschaft (DFG, German Research Foundation) -Project-ID 426888090-SFB 1441 (projects A4 and B3).

## Conflicts of Interest

The authors declare no conflicts of interest.

## Data Availability Statement

The data that support the findings of this study are available from the corresponding author upon reasonable request.

## References

1. C. Walkey, S. Das, S. Seal, et al., "Catalytic Properties and Biomedical Applications of Cerium Oxide Nanoparticles," *Environmental Science: Nano* 2, no. 1 (2015): 33–53.
2. Y. Bai, Y. Li, Y. Li, and L. Tian, "Advanced Biological Applications of Cerium Oxide Nanozymes in Disease Related to Oxidative Damage," *ACS Omega* 9 (2024): 8601–8614.
3. F. Corsi, E. Di Meo, D. Lulli, et al., "Safe-Shields: Basal and Anti-UV Protection of Human Keratinocytes by Redox-Active Cerium Oxide Nanoparticles Prevents UVB-Induced Mutagenesis," *Antioxidants* 12, no. 3 (2023): 757.
4. B. G. Seo, J. Koo, H. J. Jeong, H. W. Park, N. I. Kim, and J. H. Shim, "Performance Enhancement of Polymer Electrolyte Membrane Fuel Cells with Cerium Oxide Interlayers Prepared by Aerosol-Assisted Chemical Vapor Deposition," *ACS Sustainable Chemistry & Engineering* 11, no. 29 (2023): 10776–10784.
5. F. S. Cursi, L. Grimaud, J. Rousseau, et al., "Selective Glycerol-to-Glycerate Electro-Oxidation on Cerium-Modified Pt/C Nanocatalyst in an Alkaline Direct Alcohol Fuel Cell: Cogeneration of Energy and Value-Added Products," *ChemElectroChem* 11, no. 3 (2024): e202300555.
6. A. John-Herpin, A. Tittl, L. Kühner, et al., "Metasurface-Enhanced Infrared Spectroscopy: An Abundance of Materials and Functionalities," *Advanced Materials* 35, no. 34 (2023): 2110163.
7. C. Wöll, "Structure and Chemical Properties of Oxide Nanoparticles Determined by Surface-Ligand IR Spectroscopy," *ACS Catalysis* 10, no. 1 (2019): 168–176.
8. C. Yang and C. Wöll, "Infrared Reflection-Absorption Spectroscopy (IRRAS) Applied to Oxides: Ceria as a Case Study," *Surface Science* 749 (2024): 122550.
9. J. Acquarelli, T. van Laarhoven, J. Gerretzen, T. N. Tran, L. M. Buydens, and E. Marchiori, "Convolutional Neural Networks for Vibrational Spectroscopic Data Analysis," *Analytica Chimica Acta* 954 (2017): 22–31.
10. S. Malek, F. Melgani, and Y. Bazi, "One-Dimensional Convolutional Neural Networks for Spectroscopic Signal Regression," *Journal of Chemometrics* 32, no. 5 (2018): e2977.
11. N. Nitika, B. Keerthiveena, G. Thakur, and A. S. Rathore, "Convolutional Neural Networks Guided Raman Spectroscopy as a Process Analytical Technology (PAT) Tool for Monitoring and Simultaneous Prediction of Monoclonal Antibody Charge Variants," *Pharmaceutical Research* 41 (2024): 463–473.
12. D. Punjabi, Y.-C. Huang, L. Holzhauer, et al., "Infrared Spectrum Analysis of Organic Molecules with Neural Networks Using Standard Reference Data Sets in Combination with Real-World Data," *Journal of Cheminformatics* 17, no. 1 (2025): 1–13.
13. C. Yang, H. Idriss, Y. Wang, and C. Wöll, "Surface Structure and Chemistry of CeO<sub>2</sub> Powder Catalysts Determined by Surface-Ligand Infrared Spectroscopy (SLIR)," *Accounts of Chemical Research* 57, no. 22 (2024): 3316–3326.
14. C. Yang, X. Yu, S. Heißler, et al., "Surface Faceting and Reconstruction of Ceria Nanoparticles," *Angewandte Chemie International Edition* 56, no. 1 (2017): 375–379.
15. F. Maurer, J. Jelic, J. Wang, et al., "Tracking the Formation, Fate and Consequence for Catalytic Activity of Pt Single Sites on CeO<sub>2</sub>," *Nature Catalysis* 3, no. 10 (2020): 824–833.
16. A. Chen, X. Yu, Y. Zhou, et al., "Structure of the Catalytically Active Copper-Ceria Interfacial Perimeter," *Nature Catalysis* 2, no. 4 (2019): 334–341.
17. D. Gashnikova, F. Maurer, E. Sauter, et al., "Highly Active Oxidation Catalysts through Confining Pd Clusters on CeO<sub>2</sub> Nano-Islands," *Angewandte Chemie International Edition* 63, no. 35 (2024): e202408511.
18. H.-Y. Yu, B. Muthiah, S.-C. Li, W.-Y. Yu, and Y.-P. Li, "Surface Characterization of Cerium Oxide Catalysts Using Deep Learning with Infrared Spectroscopy of Co," *Materials Today Sustainability* 24 (2023): 100534.
19. M. V. Ganduglia-Pirovano, A. Martínez-Arias, S. Chen, Y. Wang, and P. G. Lustemberg, "Comment on "Surface Characterization of Cerium Oxide Catalysts Using Deep Learning with Infrared Spectroscopy of CO," *Materials Today Sustainability* 26 (2024): 100783.
20. A. Saghi, R. Junjuri, L. Lensu, and E. M. Vartiainen, "Semi-Synthetic Data Generation to Fine-Tune a Convolutional Neural Network for Retrieving Raman Signals from CARS Spectra," *Optics Continuum* 1, no. 11 (2022): 2360–2373.
21. T. A. Teklemariam, F. Chou, P. Kumaravel, and J. Van Buskrik, "Art - Ftir Spectroscopy and Machine/Deep Learning Models for Detecting Substitutions in Coconut Water with Sugars, Sugar Alcohols, and Artificial Sweeteners. Deep Learning Models for Detecting Substitutions in Coconut Water with Sugars," *Sugar Alcohols, and Artificial Sweeteners*, 322 (2023).
22. X. Xin, J. Jia, S. Pang, et al., "Combination of Near-Infrared Spectroscopy with Wasserstein Generative Adversarial Networks for Rapidly Detecting Raw Material Quality for Formula Products," *Optics Express* 32, no. 4 (2024): 5529–5549.
23. L. Caulfield, E. Sauter, H. Idriss, Y. Wang, and C. Wöll, "Bridging the Pressure and Materials Gap in Heterogeneous Catalysis: A Combined UHV, in Situ, and Operando Study Using Infrared Spectroscopy," *The Journal of Physical Chemistry C* 127, no. 29 (2023): 14023–14029.



24. P. G. Lustemberg, C. Yang, Y. Wang, C. Wöll, and M. V. Ganduglia-Pirovano, "Vibrational Frequencies of CO Bound to All Three Low-Index Cerium Oxide Surfaces: A Consistent Theoretical Description of Vacancy-Induced Changes Using Density Functional Theory," *The Journal of Chemical Physics* 159, no. 3 (2023): 034704,
25. P. G. Lustemberg, P. N. Plessow, Y. Wang, et al., "Vibrational Frequencies of Cerium-Oxide-Bound CO: A Challenge for Conventional DFT Methods," *Physical Review Letters* 125, no. 25 (2020): 256101.
26. W. Wu, L. M. Savereide, J. Notestein, and E. Weitz, "In-Situ IR Spectroscopy as a Probe of Oxidation/Reduction of Ce in Nanostructured CeO<sub>2</sub>," *Applied Surface Science* 445 (2018): 548–554.
27. S. Afrin and P. Bollini, "On the Utility of Ce<sup>3+</sup> Spin–Orbit Transitions in the Interpretation of Rate Data in Ceria Catalysis: Theory, Validation, and Application," *The Journal of Physical Chemistry C* 127, no. 1 (2022): 234–247.
28. D. Salusso, S. Mauri, G. Deplano, P. Torelli, S. Bordiga, and S. Rojas-Buzo, "MOF-Derived CeO<sub>2</sub> and CeZrO<sub>x</sub> Solid Solutions: Exploring Ce Reduction through FTIR and NEXAFS Spectroscopy," *Nanomaterials* 13, no. 2 (2023): 272.
29. T. Alammar, H. Noei, Y. Wang, W. Grünert, and A.-V. Mudring, "Ionic Liquid-Assisted Sonochemical Preparation of CeO<sub>2</sub> Nanoparticles for CO Oxidation," *ACS Sustainable Chemistry & Engineering* 3, no. 1 (2015): 42–54.
30. H. Idriss and J. Llorca, "Low Temperature Infrared Study of Carbon Monoxide Adsorption on Rh/ceo<sub>2</sub>," *Catalysts* 9, no. 7 (2019): 598.
31. M. Manzoli, F. Vindigni, T. Tabakova, et al., "Structure-Reactivity Relationship in Co<sub>3</sub>O<sub>4</sub> promoted Au/CeO<sub>2</sub> Catalysts for the CH<sub>3</sub>OH Oxidation Reaction Revealed by in Situ FTIR and Operando EXAFS Studies," *Journal of Materials Chemistry A* 5, no. 5 (2017): 2083–2094.
32. L. Caulfield, E. Sauter, H. Idriss, and C. Wöll, "Tracking the Redox Properties of CeO<sub>2</sub> Powders by Infrared Spectroscopy: Monitoring the Defect States by O<sub>2</sub> Adsorption and the Ce<sup>3+</sup> Spin-Orbit Transition," *The Journal of Physical Chemistry C* 129, no. 2 (2024): 1228–1233.
33. J. Wang, E. Sauter, A. Nefedov, et al., "Dynamic Structural Evolution of Ceria-Supported Pt Particles: A Thorough Spectroscopic Study," *The Journal of Physical Chemistry C* 126, no. 21 (2022): 9051–9058.
34. S. Chen, P. N. Pleßow, Z. Yu, et al., "Structure and Chemical Reactivity of Y-Stabilized ZrO<sub>2</sub> Surfaces: Importance for the Water-Gas Shift Reaction," *Angewandte Chemie International Edition* 63, no. 27 (2024): e202404775.
35. J. L. Lansford and D. G. Vlachos, "Infrared Spectroscopy Data-and Physics-Driven Machine Learning for Characterizing Surface Microstructure of Complex Materials," *Nature Communications* 11, no. 1 (2020): 1513.